



Base flow dependence on nozzle cluster configuration during ascent for a VTVL launcher

Tamás Bvkerk 1

Abstract

This study investigates the influence of nozzle cluster configuration on the base flow during ascent in a simplified reusable launcher geometry. Three engine cluster layouts, featuring 7, 9, and 33 nozzles, were analyzed using CFD at selected points along the ascent trajectory. The results indicate that the 7- and 9-engine configurations exhibit similar base flow characteristics, including recirculation patterns, base pressure, and heat flux distributions. In contrast, the 33-engine configuration demonstrates distinct differences in these flow phenomena. These findings highlight the impact of nozzle arrangement on plume-plume interactions and flow separation behavior across varying Mach numbers. Future work will focus on evolving base configurations, incorporating recent design innovations such as recessed nozzles and structural fairings, to further assess their aerodynamic and thermal effects.

Keywords: CFD, ascent, launcher, aerodynamics, heat flux, nozzle cluster, reusability

1. Introduction

Engine clustering is a common design choice for launch vehicles. Figure 1 presents some notable modern examples, including SpaceX's Falcon 9, which uses nine Merlin engines on its first stage, Blue Origin's New Glenn with seven BE-4 engines, and SpaceX's Starship Super Heavy booster with 33 Raptor engines [1]. This approach is not limited to reusable rockets; for instance, Soyuz and the Space Launch System utilize four-engine clusters, while smaller launchers like Rocket Lab's Electron employ nine-engine clusters to achieve orbital performance. Clustering offers several advantages: smaller thrust chambers are generally easier to manufacture, especially with additive manufacturing; redundancy enables continued operation after engine failures; and distributed gimbaling enhances control authority. Additionally, specific engines can be re-ignited for re-entry and landing burns, which require only a fraction of ascent thrust. These benefits have driven the widespread adoption of engine clustering across various vehicle sizes and mission profiles.

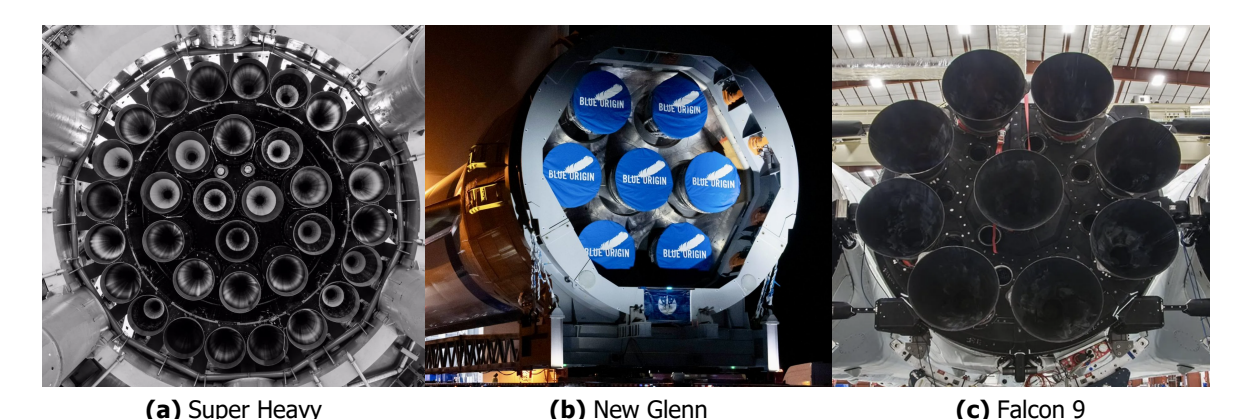


Fig 1. Examples of various engine arrangments

HiSST-2025-0010 Copyright © 2025 by the author(s)

¹DLR - Deutsches Zentrum für Luft- und Raumfahrt, AS-RFZ, Göttingen, tamas.bykerk@dlr.de

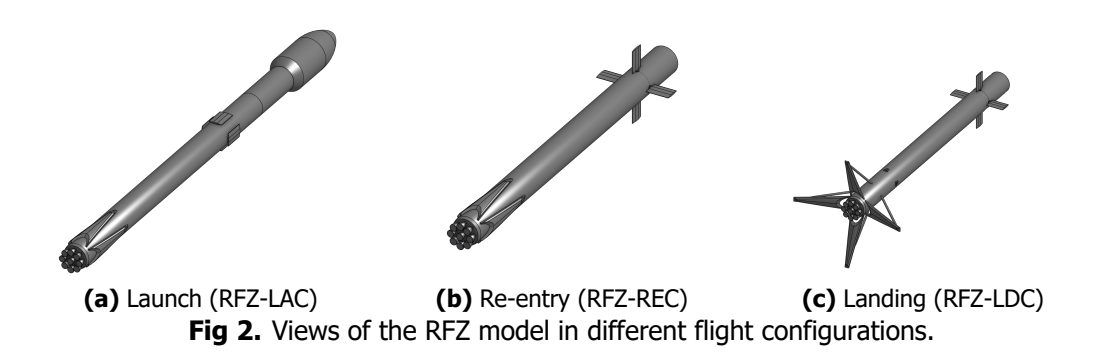
The base flow resulting from different engine cluster configurations strongly influences aerodynamic performance through base drag, as well as thermal protection system loads due to convective and radiative heat fluxes. In clustered configurations, these effects are shaped not only by exhaust—freestream interactions but also by complex plume—plume interactions, especially during high-altitude flight where plume expansion is severe. These interactions alter the size and shape of recirculation zones, as well as modify pressure and heat flux distributions at the base of the vehicle.

This study examines three engine cluster layouts at selected points along an ascent trajectory. The baseline 9-engine configuration is compared with alternative arrangements featuring 7 and 33 nozzles, with a focus on understanding the flow behavior and thermal impacts associated with each layout.

2. Geometric Details

2.1. RFZ Model

The vehicle used for this study is the DLR RFZ model, an open-source model used in studies related to reusable launchers, nozzle flows, and high-altitude aerodynamics [2, 3, 4, 5, 6]. Multiple configurations for the vehicle exist, with the launch, re-entry, and landing configurations presented in Figure 2. A comprehensive overview is available in [7], and the geometries, trajectory and results from previous studies accessible via ref. [8].



A modified version of the RFZ-LAC configuration is used, with the landing legs and planar fins removed to simplify surface geometry and reduce grid complexity. The baseline 9-engine layout is shown in Figure 3.

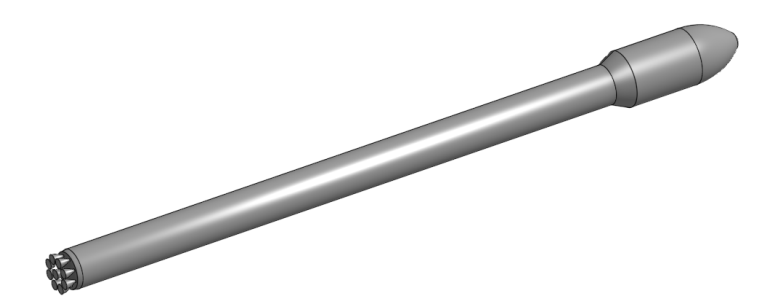


Fig 3. Simplified RFZ geometry

The three nozzle configurations (Figure 4) maintain consistent outer ring positioning so that the nozzle exit radial extent remains unchanged. This ensures that each nozzle in the outer ring protrudes the same distance relative to the baseplate lip. The 33-engine setup exhibits a near-continuous ring of nozzles with minimal gaps, while the middle ring of nozzles is located closer to the central nozzles, which are organised triangluarly. These observations are based on publicly available photos of the SpaceX Super Heavy booster.

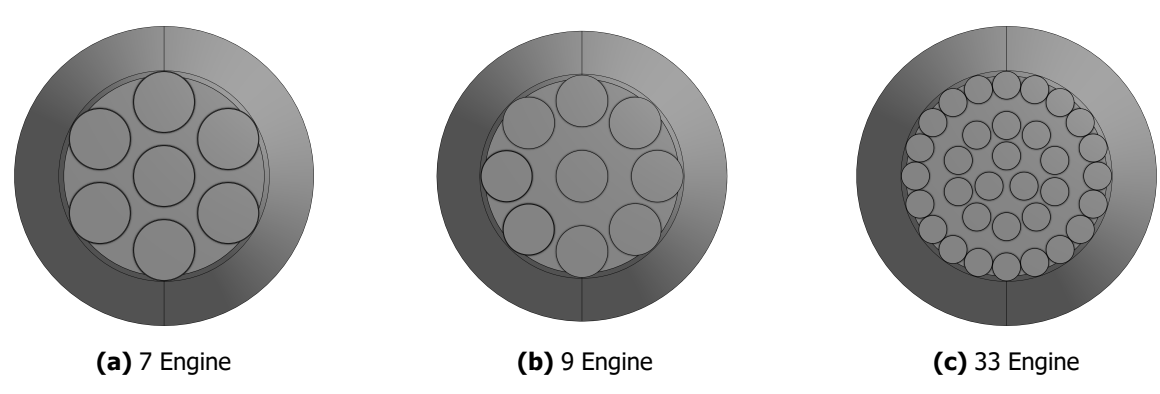


Fig 4. Overview of nozzle arrangements

2.2. Nozzle Design

The baseline nozzle is adapted from the Merlin 1D engine, operating on kerosene-liquid oxygen (kerolox) with a nominal O/F ratio of 2.35 and chamber pressure of 108 bar. Figure 5 summarizes the dimensions.

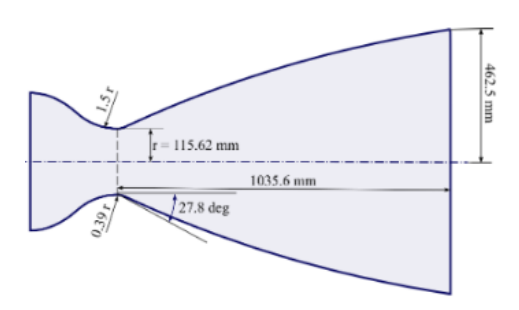


Fig 5. Baseline nozzle dimensions

In the engine variation cases, chamber conditions and nozzle expansion ratios remain fixed. The nozzles in the 7-engine configuration are scaled up in diameter, while those in the 33-engine setup are scaled down. Scaling factors are based on mass flow rates, ensuring that the total thrust from all engines remains equal. A detailed list of engine parameters is provided in Table 1.

	·		·
Parameter	7 Engines	9 Engines	33 Engines
Total temperature (K)	3645.51	3645.51	3645.51
Total pressure (bar)	108	108	108
Exit pressure (bar)	0.76462	0.76462	0.76462

250.97

0.04200

0.67200

68.44

0.01145

0.18327

322.67

0.05400

0.86400

Table 1. Engine parameters based on CEA outputs

It should be noted that the assumption of constant chamber pressure and thermodynamic conditions across all engine sizes is a simplification. In reality, scaling an engine significantly, either up or down, can affect factors such as heat transfer, injector performance, combustion efficiency, and cooling requirements. Nevertheless, for the purposes of this study, the goal is to isolate and understand the

HiSST-2025-0010

Mass flow (kg/s)

Throat area (m²)

Exit area (m²)

aerodynamic effects of nozzle layout on base drag and flow structure. To enable a controlled comparison, it was necessary to keep the engine operating conditions consistent across all configurations, even if this assumption introduces some idealization.

3. Numerical Setup

3.1. DLR TAU Code

The TAU code is a second-order finite volume solver for the Euler and Navier–Stokes equations, offering a broad selection of RANS-based and scale-resolving turbulence models. It is designed for use with unstructured computational grids, enabling simulations over complex geometries, and is highly optimized for massively parallel high-performance computing environments. TAU has been extensively validated and applied across a wide range of subsonic to hypersonic flows, including ascent configurations for reusable launch vehicles [9].

For this study, TAU is applied to investigate aerodynamic and base flow phenomena during ascent, where nozzle plume expansion and plume-freestream interactions dominate the flow near the vehicle base. Inviscid fluxes are computed using the AUSMDV flux vector splitting scheme, combined with MUSCL gradient reconstruction to ensure second-order spatial accuracy, while turbulence is modeled using the single equation Spalart-Allmaras RANS model.

3.2. Grid and Boundary Conditions

To accurately capture near-wall behavior and heat fluxes, prismatic sub-layers are used near solid boundaries, with a first-cell non-dimensional wall spacing of $y^+\approx 1$ and a wall-normal stretching ratio < 1.3. A constant wall temperature of 300 K is prescribed. The computational domain is spherical, extending approximately 20 vehicle lengths upstream and downstream from the vehicle centerline to minimize boundary influence at subsonic Mach numbers and allow enough computational domain to capture the plume. In each case, localized mesh refinement is applied around the vehicle body and base region to resolve key features of the flow. All numerical grids exploit symmetry. The symmetry planes vary according to the configuration tested, with a 1/16, 1/12 and 1/2 domain slice used to model the 9, 7 and 33 engine layouts respectively. All simulations were conducted at an angle of attack equal to zero.

For the baseline geometry, 12 trajectory points were selected to cover the entire ascent trajectory from launch up to staging. For the engine variation cases, half were considered for comparison. Table 2 gives an overview of the trajectory points, with the variation and baseline cases marked.

Time (s)	Temperature (K)	Pressure (Pa)	Mach Number (-)	Baseline	Variations
24.00	281.71	90509.00	0.30	Х	Х
35.00	272.08	75218.40	0.52	Х	Х
47.00	256.22	55017.60	0.82	Х	Х
51.00	249.40	47436.60	0.95	Х	
56.00	239.97	39005.30	1.06	Х	
61.00	230.27	31441.00	1.20	Х	Х
65.00	222.30	25435.00	1.35	Х	
72.00	216.60	17308.00	1.62	Х	
91.00	217.80	4639.80	2.52	Х	
116.00	239.02	506.75	4.06	Х	X
136.00	269.00	62.21	5.53	Х	
147.00	238.48	14.44	7.07	Х	Х

Table 2. Selected trajectory points for baseline and variation cases

3.3. Plume Modeling

Due to the presence of high-temperature exhaust gases, the standard solver setup using air with a ratio of specifics heat equal to 1.4 is no longer valid. In these cases, the CFD setup employs a two-species model, treating the atmospheric air and nozzle exhaust as distinct, chemically frozen, and thermally perfect gas mixtures—each with their own thermodynamic and transport properties.

The atmospheric air is assumed to consist of 77% N2 and 23% O2 by mass, while the exhaust composition is based on prior work [7]. The resulting mass fractions used for the nozzle exhaust are: CO (37.4%), CO2 (35.5%), H2 (1.2%), and H2O (25.9%). All thermodynamic properties of the air and plume species are precomputed and tabulated using an in-house tool which incorporates data from the NASA polynomials [10].

This two-species, frozen-composition model avoids the high computational cost of solving chemical kinetics, but it also introduces limitations. Notably, it cannot account for post-combustion reactions or non-equilibrium chemical processes that may occur in the shear layer between the plume and ambient air [9]. Nonetheless, the approach is considered adequate for capturing the dominant momentum and thermal interactions relevant to base flow behavior during ascent.

4. Results and Discussion

4.1. Baseline Configuration

Figure 6 presents an overview of the total vehicle drag over the investigated Mach number range. Drag coefficient is seen to decrease slightly between Mach 0.3 and 0.8, before strongly increasing through the transonic range. A peak drag coefficient is recorded at Mach 1.35 before swiftly decreasing. At approximately Mach 5.5, the drag coefficient transitions from positive to negative. This trend continues down to Mach 7, the maximum Mach number investigated.

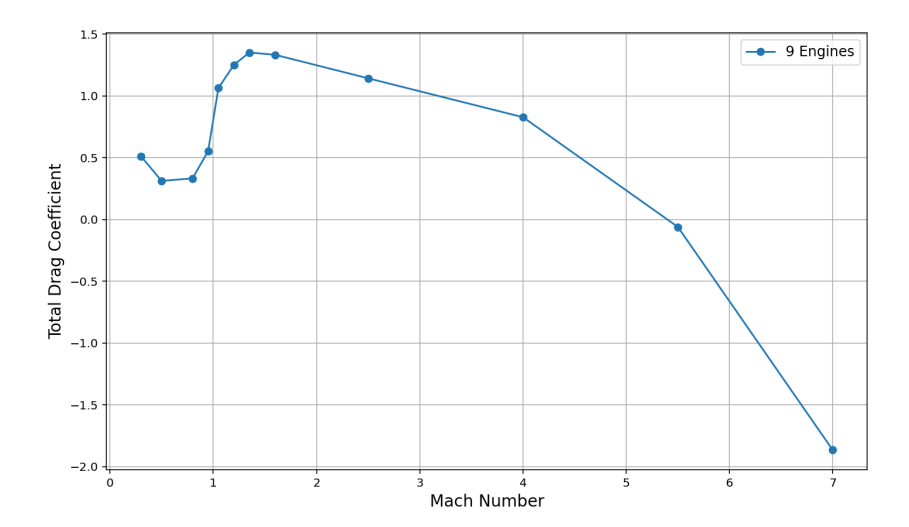


Fig 6. Total drag coefficient as a function of Mach number for the baseline 9 engine configuration

To better understand the phenomena seen in the total drag coefficient data, a component level break-down is provided in Figure 7. The wall group contains the fairing and vehicle sidewall boundaries, while the boattail refers to the slight taper transition between the vehicle sidewall and the baseplate. The baseplate refers to the flat disk where the engines are mounted, while the nozzles consider only their external walls. It is clear that the wall boundary contribution approximately follows the global trend, with a large increase in drag through the transonic region. The baseplate and nozzle walls exhibit both positive and negative values of drag throughout the flight. Up until Mach 2.5, the sign of the nozzle drag is the opposite of the baseplate, while at Mach 4 and above, both the nozzles and baseplate exhibit strongly negative drag. In fact, the magnitude of the negative drag (thrust), is so high that it overcomes the positive wall drag, resulting in the transition from positive to negative drag seen in Figure 6. The

boattail contribution to total drag is low, which is expected given its small surface area and inclination angle to the flow.

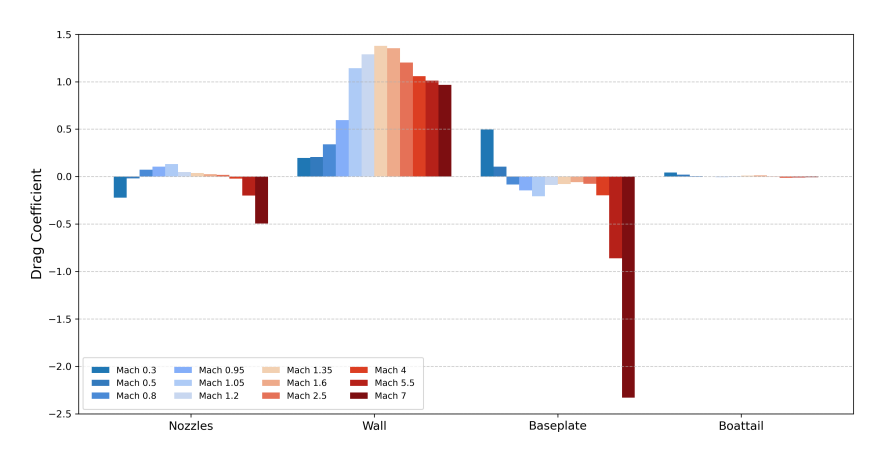


Fig 7. Drag coefficient breakdown as a function of Mach number for the baseline 9 engine configuration

It is somewhat counterintuitive to observe negative drag on the baseplate for much of the flight, especially since base drag is typically the main contributor to total drag on unpowered projectiles. However, previous studies on single-engine geometries have documented that the ratio of base pressure to freestream static pressure can shift from below 1 (base drag) to above 1 (base thrust) as thrust coefficient increases [11, 12]. This highlights the importance of nozzle exit conditions alongside freestream parameters in determining rocket base pressure. What remains less explored is the effect of clustered nozzle configurations.

Figure 8 shows Mach number contours and streamtraces at selected trajectory points, revealing key flow features. At Mach 0.3, entrainment of freestream flow into the base area is observed, causing separation without reversed nozzle flow (updraft plume). This entrained flow exits the base with exhaust gases, creating suction and significantly contributing to total vehicle drag. At Mach 0.8, a larger separation bubble forms at the baseplate lip, and the updraft plume begins to develop, overcoming entrainment and impinging on the baseplate with pressures above ambient. At Mach 7, the plume is highly underexpanded, causing strong plume—plume interactions and a supersonic updraft plume that cannot remain attached to the central nozzle walls, resulting in recirculation around the nozzle extension (see Figure 8c). Severe plume-induced flow separation (PIFS) occurs due to low ambient pressure, with the updraft plume stagnating on the baseplate before turning radially and interacting with the PIFS, forming two distinct separation bubbles.

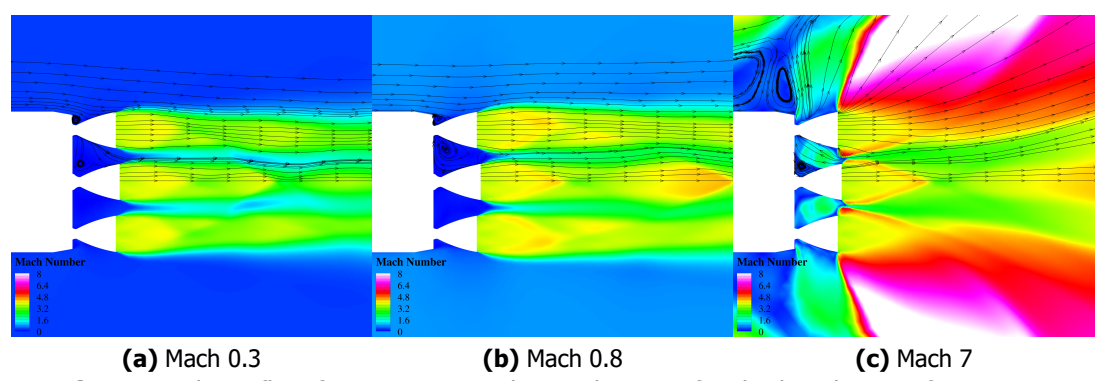


Fig 8. Key base flow features across the Mach range for the baseline configuration.

Figure 9 shows the base pressure contours for the 9-engine configuration. Because of the large variation

in pressure coefficient values across the Mach number range, unique contour scales were used for each case. At Mach 0.3, peak pressure coefficients appear on the outward-facing surfaces of the nozzle extension bases, with surrounding low-pressure regions just above the minimum pressure coefficient values. This suggests the flow separates at the baseplate lip where it meets the nozzles, then accelerates around the nozzles. The spaces between the nozzles are less constrained, allowing flow to be drawn directly behind the baseplate, which creates low-pressure areas. The pressure coefficient is mostly negative, which aligns with the positive drag contribution seen in Figure 7.

At Mach 0.8, pressure peaks occur in the center of the baseplate due to the updraft plume impinging on this area. At Mach 7, the effects of increasing plume-plume interactions are clear, with high pressure coefficients concentrated in a ring between the peripheral and central nozzles. Flow stagnation occurs along the inside-facing edges of the peripheral nozzles as the updraft plume stagnates on the baseplate and is redirected radially, impinging on the nozzle bases. The flow then accelerates and separates on the lee side of the nozzles.

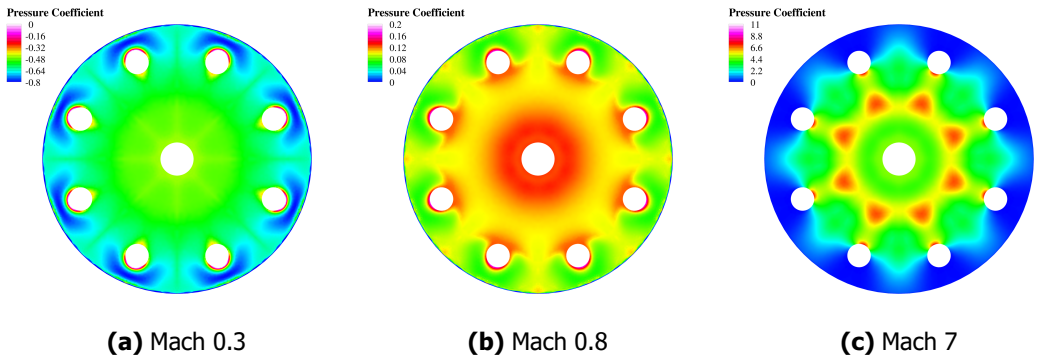


Fig 9. Base pressure coefficient across the Mach range for the baseline configuration.

The influence of the updraft plume on the base heating as freestream Mach number (and altitude) increase is illustrated in Figure 10. At Mach 0.3 and Mach 0.8, the convective heat flux remains mostly negative—indicating cooling—at the prescribed isothermal wall temperature of 300 K. At high altitudes, peak heat fluxes approaching 100 kW/m² are recorded. The hotspots are observed between the central nozzle and the peripheral nozzles, where the exhaust plumes stagnate, resulting in updraft plume and the jetting of hot exhaust gases to the baseplate. Note that while the convective heat fluxes at the lower Mach numbers as extremely small, it is during this time that radiative heat flux is expected to be at its highest [13].

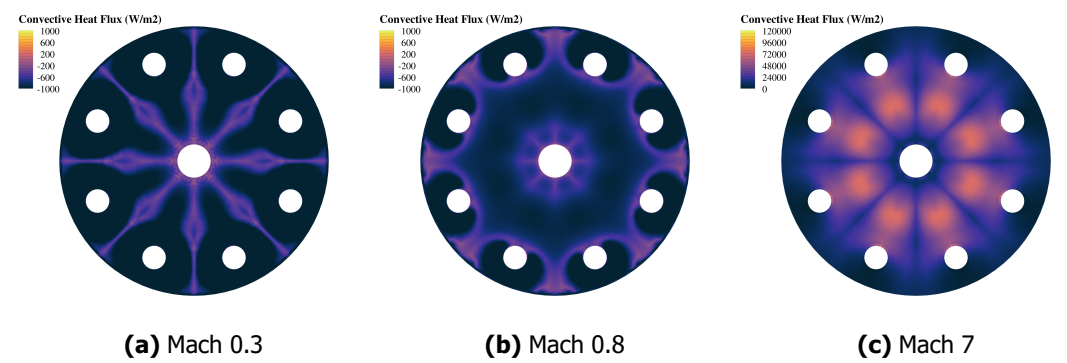


Fig 10. Base heating (convective) across the Mach range for the baseline configuration.

4.2. Comparison of Cluster Variations Against Baseline

In Figure 11, selected trajectory points for the 7 and 33 engine nozzle arrangements are compared with the baseline configuration for total drag coefficient. Generally, good agreement in the drag coefficient is seen for the baseline configuration and the 7 nozzle arrangement across the entire Mach number range. This also holds true for the 33 engine design between Mach 0.8 and 4. Outside of this range, large variances are observed.

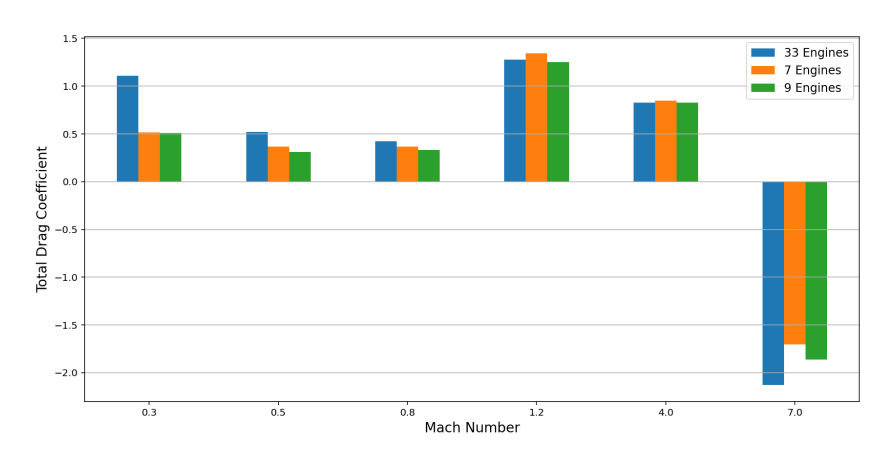


Fig 11. Total drag coefficient at selected Mach numbers for the baseline 9 engine configuration compared with 7 and 33 engine configurations

Contours of surface pressure coefficient at Mach 0.3 for the various nozzle configurations are presented in Figure 12. Note that due to the order of magnitude difference between the 33 engine configuration and the other two arrangements, a different scale was necessary. All engine configurations display similar patterns at the baseplate lip, where low pressure peaks appear around the nozzle-baseplate junctions. The lowest value of pressure coefficient is seen for the 33 engine configuration, while the highest is seen for the 7 engine arrangement. This is most likely due to the closer proximity of the nozzles to the baseplate lip, influencing the size of the recirculation region as the flow separates off the boattail. Higher pressure coefficients are located towards the centre of the baseplate in all cases. This is due to regions of lower flow acceleration before the flow is entrained with the nozzle flow and exits the base area.

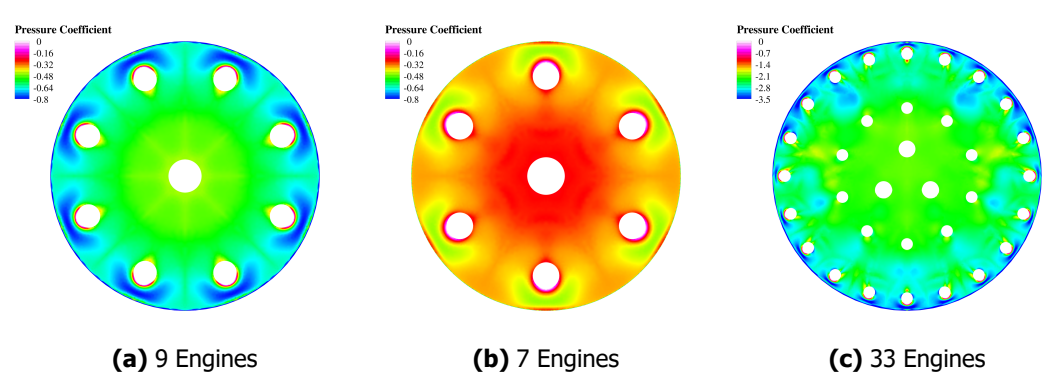


Fig 12. Base pressure coefficient at Mach 0.3 for the various engine configurations.

Contours of surface pressure coefficient at Mach 7 for the various nozzle configurations are presented in Figure 13. Recall that at this condition there is significant backflow to the base due to the low ambient pressure. The 7 engine arrangement shifts the stagnation point closer towards the peripheral nozzles, most likely due to the closer overall proximity of the nozzle exit planes to each other. This alters the

separation bubble at the base of the central nozzle and in turn, how the backflow is forced to impinge on the baseplate. The 33 nozzle configuration has three main regions of high pressure on the surface. In this configuration the contours show a largely assymetric pressure distribution, which is due to the inner three nozzle configuration. Plume-plume interactions are no longer dominated by the centre nozzle flow interacting with the outer ring nozzle flows, with the 33 engine arrangement giving rise to isolated pressure peaks created by interactions created by 3, 4 or 5 engine sub-clusters.

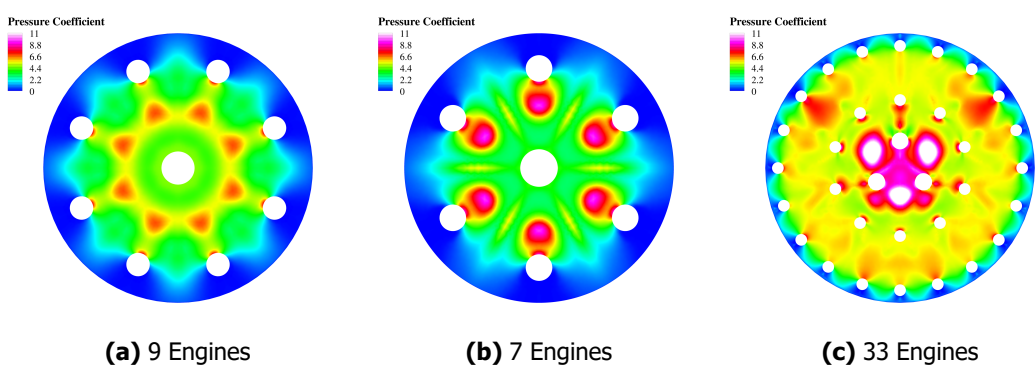


Fig 13. Base pressure coefficient at Mach 7 for the various engine configurations.

Similar to the pressure coefficient contours, the base heating footprints are complex and asymmetric for the 33 engine configuration. Pressure peaks correlate well with the locations of highest heat flux, which is consistent with stagnating, high temperature gases. The baseline case showed the lowest peak heating, with values of up to approximately 90 kW/m 2 recorded. The 7 engine configuration saw slightly higher peaks of 120 kW/m², while the highest loads were seen for the 33 engine configuration where 200 kW/m² was exceeded. These variations in surface heating can be attributed not only to differences in mass flow—both exiting the nozzles and within the updraft plume—but also to the degree of plume mixing, as well as the stagnation temperatures reached in the plume-plume interaction zones.

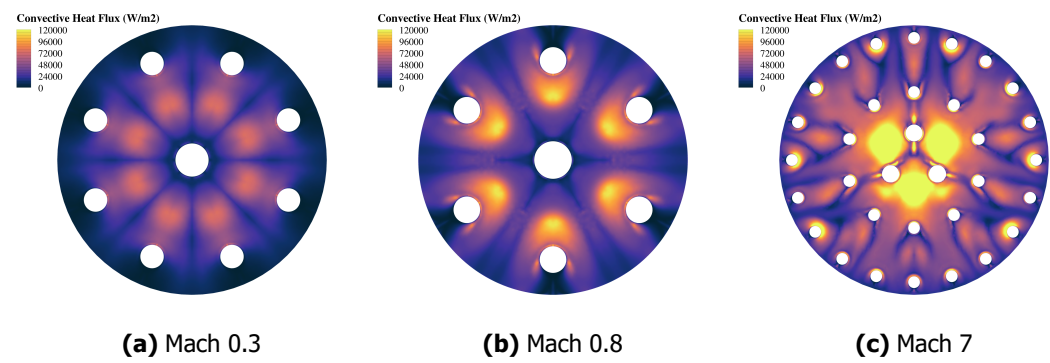


Fig 14. Base pressure coefficient at Mach 7 for the various engine configurations.

Figure 15 attempts to correlate the heatflux and pressure peaks with the flow topology through the analysis of backflow. A slice has been made at approximately 75% of the nozzle length, with only negative axial velocity plotted. Different coloured arrows indicate the nozzles from which plumes are likely interacting with each other and causing the updraft plume. Green arrows denote a 5 nozzle subcluster, with red indicating a 4 engine sub cluster and purple denoting 3 engine sub clusters. The highest negative flow velocities correlate well with where the peak heating and pressure values were recorded on the baseplate. It also highlights the possibility for heat mitigation strategies by rotating or changing radial placement of the rings to reduce the base heating.

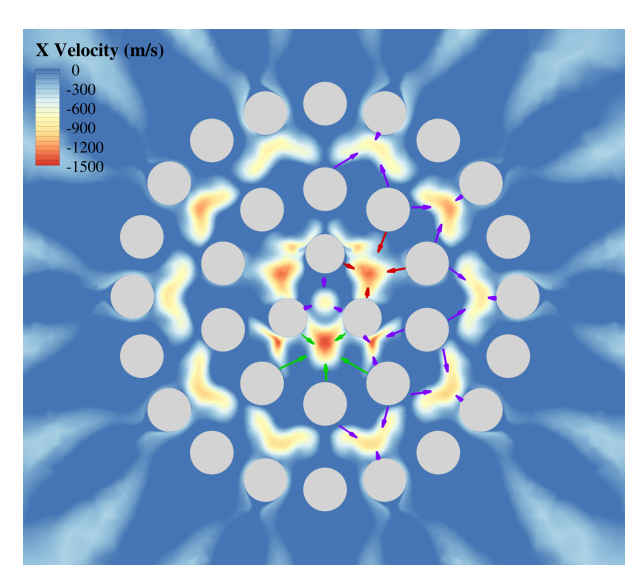


Fig 15. X velocity contour at slice in the base region

5. Summary and Future Work

This study highlights the significant impact of nozzle cluster configuration on the base flow during ascent of a VTVL launcher. Variations in nozzle layout influence flow separation, recirculation zones, base pressure, and heat flux distribution, all of which are critical for vehicle aerodynamics and the design of thermal protection systems. Notably, the 33-engine configuration exhibited large deviations in base drag compared to the baseline across both low and high Mach numbers, reflecting the complex flow dynamics introduced by dense clustering. Peak heating was also highest in this configuration, exceeding 200 kW/m², driven by intense plume—plume interactions and stagnation effects.

Future work will focus on understanding the increasingly complex base regions of reusable launch vehicles, as they evolve to meet the competing demands of aerodynamics, thermal protection, and reusability. Designs like Rocket Lab's Neutron, with its recessed nozzles and strake-integrated landing legs, Blue Origin's New Glenn, featuring a flared shroud and aerodynamic strakes, and SpaceX's Super Heavy, with its partial fairing over the outer engine ring, represent a shift away from traditional open-base configurations. These innovations introduce new flow behaviors and structural interactions that impact both ascent and descent phases. As these architectures continue to develop, there is significant value in systematically analyzing how base design choices affect plume dynamics, base drag and overall vehicle performance throughout flight.

References

- [1] T. Bykerk, S. Karl, M. Laureti, M. Ertl, and T. Ecker. Retro-propulsion in rocket systems: Recent advancements and challenges for the prediction of aerodynamic characteristics and thermal loads. *Progress in Aerospace Sciences*, 151:101044, 2024.
- [2] R. Rankin and T. Bykerk. The influence of a retro-propulsion plume on vehicle aerodynamics and aeroheating during hypersonic re-entry. In *AFMC 24*, Canberra, Australia, December 2024.
- [3] T. Bykerk and T. Horchler. The influence of a retro-propulsion plume on vehicle aerodynamics and aeroheating during hypersonic re-entry. In *AFMC 24*, Canberra, Australia, December 2024.
- [4] S. Karl, T. Bykerk, and M. Laureti. Design of a truncated ideal nozzle for a re-usable first stage launcher. In *HiSST: 3rd International Conference on High Speed Vehicle Science and Technology*, Busan, Korea, April 2024.

- [5] L. Basov, M. Ertl, and T. Bykerk. Comparison of fokker-planck and cfd simulations of the rfzst2 upper stage. In HiSST: 3rd International Conference on High Speed Vehicle Science and Technology, Busan, Korea, April 2024.
- [6] M. Ertl and T. Bykerk. A standard model for the investigation of aerodynamic and aerothermal loads on a re-usable launch vehicle - second stage geometry. In HiSST: 3rd International Conference on High Speed Vehicle Science and Technology, Busan, Korea, April 2024.
- [7] T. Bykerk. A standard model for the investigation of aerodynamic and aerothermal loads on a re-usable launch vehicle. In 10th EUCASS - 9th CEAS Conference, Lausanne, Switzerland, July 2023.
- [8] T. Bykerk. The rfz model a standard model for the investigation of aerodynamic and aerothermal loads on a re-usable launch vehicle. zenodo, Jul 2023.
- [9] M. Laureti and S. Karl. Aerothermal databases and load predictions for retro propulsion-assisted launch vehicles (retalt). CEAS Space Journal, 14:501-515, 2022.
- [10] B J. McBride and S. Gordon. Nasa glenn coefficients for calculating thermodynamic properties of individual species. NASA Technical Paper NASA/TP-2002-211556, NASA Glenn Research Center, 2002.
- [11] F. G. Moore and T. C. Hymer. Improved semi-empirical method for power-on base-drag prediction. Journal of Spacecraft and Rockets, 39(1):56–65, January/February 2002.
- [12] F. G. Moore and L. Y. Moore. Improvements to power-on base pressure prediction for the aeroprediction code. Journal of Spacecraft and Rockets, 47(1):101–112, January/February 2010.
- [13] J. Kim. Pre- and postflight thermal analysis of test launch vehicle fuselage. Journal of Spacecraft and Rockets, 56(6):1786-1794, 2019.

HiSST-2025-0010